

# Sensorizing High-Aspect-Ratio Soft Robots: Towards Closed-Loop Applications for Grasping and Locomotion

Tobias Geissenberger<sup>1,2,3</sup>, Elio Challita<sup>2</sup>, Mirco Theile<sup>1</sup>, Robert J. Wood<sup>2</sup> and Justin Werfel<sup>2</sup>

**Abstract**—High aspect ratios are a common feature in biological systems like muscle fibers, tentacles, or annelids that inspire novel applications in artificial muscles, grasping, manipulation, and locomotion. This paper explores interoceptive and exteroceptive sensing methods for high-aspect-ratio soft robots to overcome the limitation of externalized sensing and control, which is currently typical for such robots. We present a design and manufacturing process for sensorized soft robots (aspect ratio  $\sim 17$ ) with an integrated stretchable carbon microparticle proprioception sensor and phototransistor-based exteroceptive layer for low-resolution ambient light detection. We show that our interoceptive sensor provides accurate results for curling during 120 pressurization cycles. The exteroceptive sensor detects the proximity of other robots but shows only a slight correlation during entanglement tests. Finally, we demonstrate that sensorized high-aspect-ratio soft robots can detect the disentanglement of robots under load.

## I. INTRODUCTION

Soft pneumatic actuators have found increasing popularity in the field of bioinspired engineering [1], [2], [3], enabling or improving performance in various applications that depend on compliance [4]. Recent work highlighted applications for high-aspect-ratio soft robots, which are well suited for delicate tasks that require low forces or high contact surfaces, including in domains such as grasping [5], manipulation [6], locomotion [7], or artificial muscles [8].

Emerging applications that leverage high-aspect-ratio soft robots are so far limited by the lack of sensory information providing feedback on the robot’s configuration. This limitation thus necessitates an external component of the system to provide state estimation and control. However, for an autonomous system not limited by the need for such external infrastructure, onboard state sensing is crucial to close the control loop.

Our work investigates interoceptive and exteroceptive embedded sensor methods for high-aspect-ratio soft robots, which we define as robots with an aspect ratio higher than 10. We extend previous one-channel designs to two pneumatic channels for richer actuation capabilities, such as antagonistic actuation, and actively controlled uncurling and curling. We propose a design and sequential molding manufacturing process for a sensorized high-aspect-ratio soft robot, which

addresses the need for onboard state sensing in such autonomous systems. Proprioceptive sensing is provided by the integration of a strain sensor based on conductive carbon microparticles in a stretchable channel. Proximity sensing is provided by the integration of a set of phototransistors to evaluate the presence of external objects at low spatial resolution along the length of the robot. We characterize the mechanical effect that the sensors impose on the robot’s actuation. We close by outlining two applications of grasping and locomotion in which sensorized high-aspect-ratio soft robots provide the potential for closed-loop autonomy.

## II. RELATED WORK

High-aspect-ratio soft robots are used in the context of grasping, either inspired by single filaments, such as elephant trunks [9], tendrils [10], [11] and tentacles [12], or collective gripping based on entanglement of multiple filaments [5]. Another context in which such robots appear is collective locomotion, as in a system inspired by California blackworms [13] where individual robots entangle into a “blob” which is itself mobile [7]. Novel manufacturing techniques for high-aspect-ratio soft robots include bubble casting [8] and dip coating [14]. This previous work concerns robots equipped with a single pneumatic channel, able to transition between curled and straight states by pressurizing and depressurizing.

Most soft robots lack sensorization and, thus, are controlled in an open loop. However, this limits the robots’ applications and requires a human operator or other external infrastructure to provide sensory input. Instead, full autonomy necessitates intero- and exteroceptive sensing that is directly integrated into the robot. Interoceptive sensing methods for soft and wearable robotics include carbon nanotube or carbon particle strain sensors [15], hydrogel strain sensors [16], optical bending sensors [17], and capacitive proprioception sensors [18]. Exteroceptive sensors for soft robots have their main applications in tactile and proximity sensing using capacitive sensors [19]. Capacitive sensors serve as self-capacitive sensors for proximity detection as well as mutual capacitive sensors for force detection [20].

Previous research has introduced interoceptive sensing for object detection in contexts such as dexterous grasping with a hand-inspired gripper [21] (with relatively large fingers and a limited aspect ratio). However, sensing in high-aspect-ratio soft robot applications remains an unresolved challenge since the small wall thicknesses required for the actuation of high-aspect-ratio robots complicate the integration of sensors into a manufacturing process for these robots. Furthermore, high-aspect-ratio soft robots can undergo strains exceeding 100%,

<sup>1</sup>School of Engineering and Design, Technical University of Munich, 80333 Munich, Germany {tobias.geissenberger, mirco.theile}@tum.de

<sup>2</sup>John A. Paulson School of Engineering and Applied Sciences, Harvard University, Boston, MA 02134, USA {echallita, rjwood, jkwerfel}@seas.harvard.edu

<sup>3</sup>School of Engineering, Ecole Polytechnique Fédérale de Lausanne, 1015 Lausanne, Switzerland

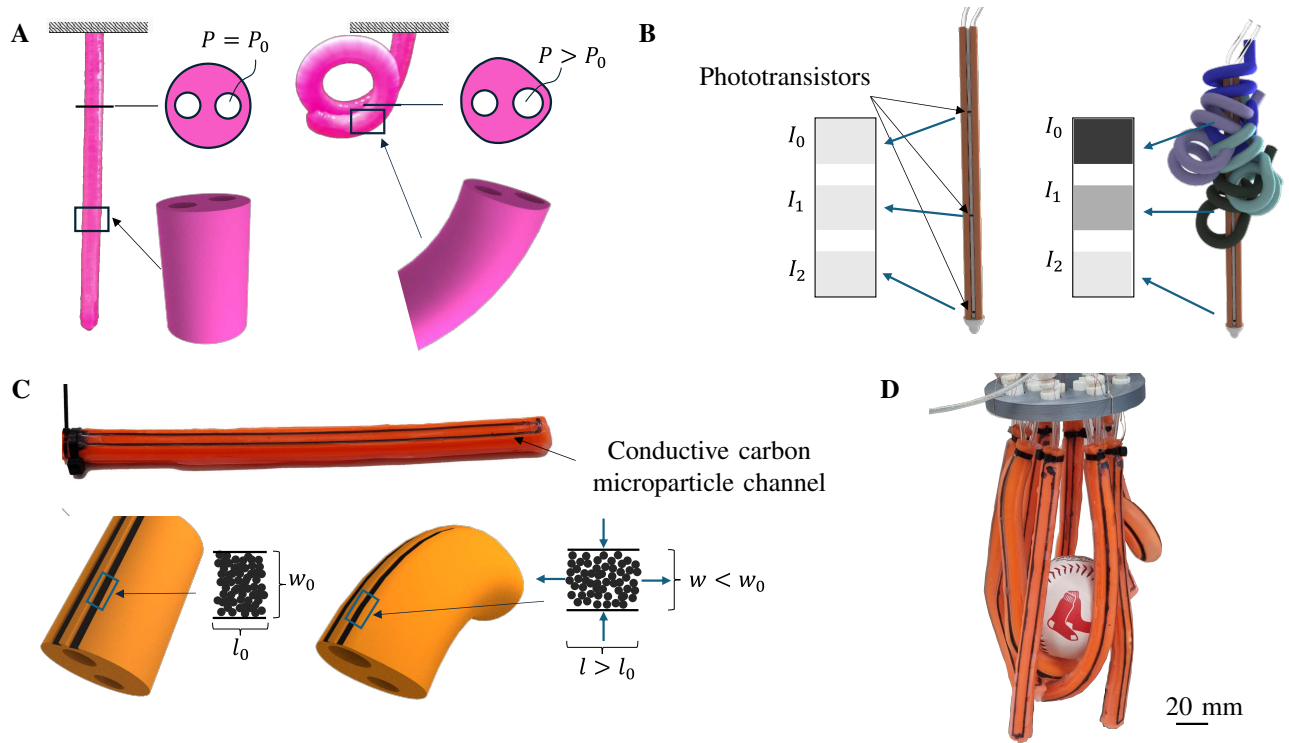


Fig. 1: Proximity and proprioception sensors for high-aspect-ratio soft pneumatic actuators. (A) Schematic of a two-channel high-aspect-ratio soft pneumatic actuator. When one channel is pressurized, the robot curls in the opposite direction. (B) Low-resolution imaging via a phototransistor array, giving information on the local presence of external objects, such as other robots in an entanglement context. (C) Proprioceptive sensor via integrated carbon microparticle channels, giving information on deformation state, based on changes in electrical resistance. (D) Entanglement of an object with a sensorized stochastic entanglement gripper.

which are significantly larger than for traditional soft robots, putting more strenuous demands on integrated hardware.

### III. MANUFACTURING SENSORIZED HIGH-ASPECT-RATIO SOFT ROBOTS

High-aspect-ratio soft robots are designed as slender elastic filaments that bend under internal pressure. We use sequential casting as the manufacturing process for these actuators, allowing us to integrate two pneumatic channels for antagonistic actuation along with sensor structures directly into the silicone cast. Figure 2 outlines the three steps to manufacture sensorized soft robots with an aspect ratio of  $\sim 17$ . The robots consist of three layers: a layer for exteroception sandwiched between two identical layers for interoception and actuation.

*A) Interoceptive Layer:* A printed mold (Prusa MK3S, PLA filament) with a U-shaped channel, and a metal rod, are sprayed with a thin film of mold release. The metal rod (diameter  $2\text{mm}$ ) is placed in a circular insert in the mold to create an integrated pneumatic channel for actuation. We pour silicone resin (Smooth-On Dragon Skin 10) into the mold and use a coater to remove excess resin. After curing, the actuation segment is demolded. We rotate it and deposit four layers of carbon ink (0.1 wt.% Orion Printex XE2B Beads and 99.9 wt.% isopropanol) with a syringe into the

U-shaped channel of the silicone cast. After two carbon layers, copper wires are connected with silver chloride ink (Dycotec Materials DM-SIP-2005PU) to the carbon channel. The channel is finally sealed with silicone resin.

*B) Exteroceptive Layer:* Silicone-coated stranded wires (Adafruit Silicone Cover Stranded-Core Wire 30AWG) are placed in an acrylic mask with a laser-cut sinusoidal pattern (Universal Laser VLS6.60). We apply a coating of low-viscous silicone resin (Smooth-On Ecoflex 20) on the mask to infuse the space between the wires and embed them in silicone. Two such embedded wire layers are bonded together and demolded. Phototransistors are soldered to the wire layers facing towards opposite sides. The sinusoidal pattern of the wires in the exteroceptive layer allows the layer to stretch, reducing the robot's bending stiffness.

*C) Sensorized Robots:* Interoceptive (from A) and exteroceptive (from B) layers are stacked in *A-B-A* sequence and bonded with translucent silicone resin (Dragon Skin 10). The bonded robot is dipped into resin to seal the pneumatic channels on one side. Pneumatic tubes are inserted on the other side and fixed with a zip tie. The final unactuated robot's dimensions are  $186\text{mm}$  long and  $11\text{mm}$  wide.

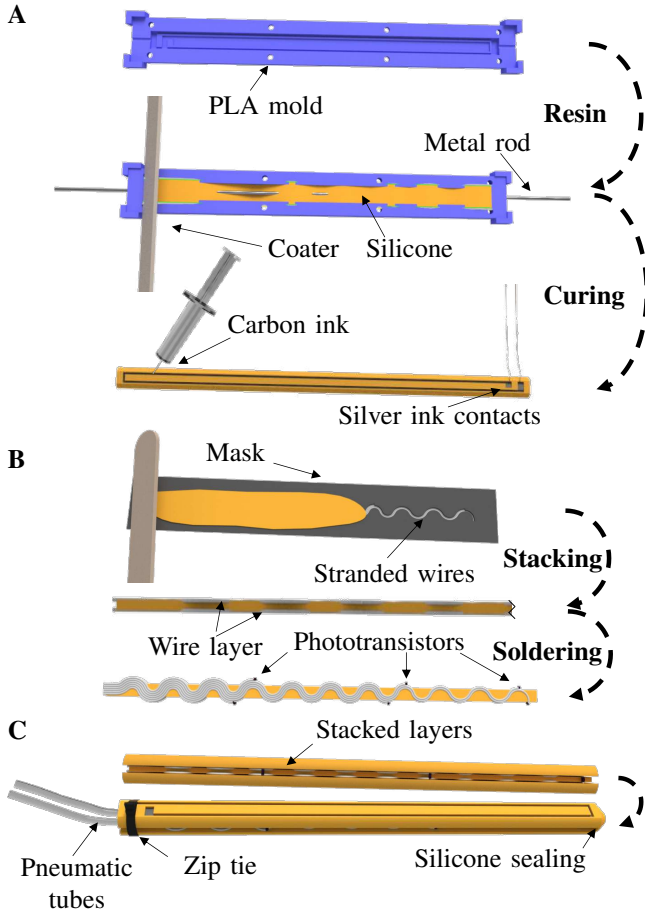


Fig. 2: Manufacturing process for sensorized high-aspect-ratio soft robots. (A) Interoceptive actuation layer with an integrated pneumatic channel and carbon microparticle strain sensor. (B) Exteroceptive layer with flexible wires and phototransistors. (C) Complete sensorized robot, stacking an exteroceptive layer between two interoceptive layers. More information on the manufacturing process is given in §III.

#### IV. SENSOR CHARACTERIZATION

##### A. Proprioception Sensor

To measure the deformation of these robots and characterize their interoceptive sensors, we manufactured several robots and tracked them with a camera system. The robot is recorded in front of a black background to obtain a binary mask by thresholding. We filter the mask with a Gaussian blur kernel, apply a closing morphology operation, and threshold it again to remove small area defects in the original mask. The mask is thinned to a pixel-wide skeleton model using a thinning algorithm [22]. We interpolate the positions of the skeleton model with piece-wise cubic splines to obtain a mathematical description of the center line of the deformed actuator as a 2D curve

$$\gamma(t) = \begin{bmatrix} x(t) \\ y(t) \end{bmatrix} \quad (1)$$

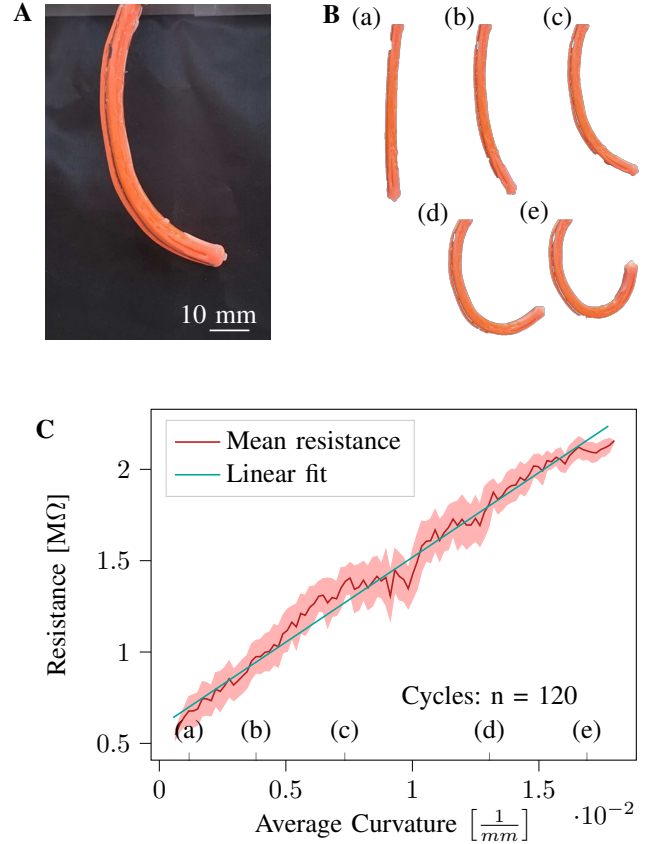


Fig. 3: Proprioceptive sensing results from integrated carbon microparticle channels. (A) Raw image of a robot with one actuation channel partially inflated. (B) Processed masked area of the deforming robot at different stages of the actuation cycle. (C) Resistive sensor measurements for a deformed high-aspect-ratio soft robot show a nearly linear bijective correlation with the tracked average curvature of the robot. The filled area shows the resistance within one standard deviation. Labels (a)–(e) correspond to the cases shown in panel B.

The curvature of the skeleton model serves as a quantitative measurement of the deformation of the robot. We approximate its deformation under a constant curvature assumption and quantify it with its average curvature. The processing steps for deformation tracking are shown in the supplementary video. We record deformations during 120 inflation cycles for one pneumatic actuator and report the average curvature and corresponding mean resistance of the carbon microparticle strain sensor measured with an LCR meter (B&K Precision 880) in Figure 3.

The long-term behavior of the sensor is tested during cyclical loading and unloading conditions. We mount a single carbon microparticle strain sensor on a tensile test machine (Instron 68TM-10) and cyclically load it to a strain of 100% for 229 cycles. The resistance  $R$  of an ideal sensor would change under assumptions of linear mechanics and a constant resistivity  $\rho$  with its strain  $\epsilon$  as

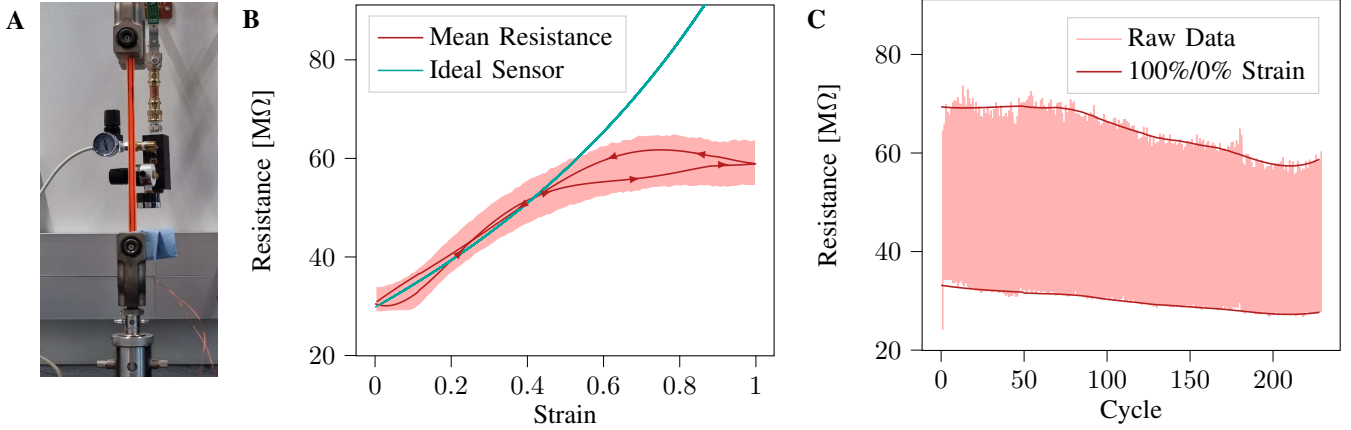


Fig. 4: Recorded data during a cyclic tensile strain test with 229 cycles on a tensile test machine (Instron 68TM-10). Data is recorded at  $2Hz$ . The sample ( $l_0 = 150mm$ ) is elongated by  $150mm$  with a constant displacement rate of  $7\frac{mm}{s}$ . (A) Carbon microparticle strain sensor clamped on the tensile test machine. (B) Mean strain-resistance relationship compared to an ideal sensor under the assumptions of linear mechanics. The empirical data shows a small hysteresis between loading and unloading cycles. The filled area indicates the interval within one standard deviation. (C) Cyclic measurements show a reduced resistance in the undeformed and deformed configurations over an increasing number of cycles.

$$R = \rho \frac{l}{wt} = \rho \frac{(1 + \epsilon)l_0}{(1 - \nu\epsilon)w_0t_0} \quad (2)$$

with  $l$  being the length of the trace,  $w$  its width,  $t$  its thickness, and  $\nu$  the Poisson ratio of the substrate. We assume that the thickness of the trace is thin such that  $t \approx t_0$ . Figure 4 compares the mean resistance from the empirical data to the ideal sensor. While the assumptions for the ideal sensor are closely followed for strains below 45%, the resistance at large strains seems to plateau. Furthermore, a small hysteresis is visible between the loading and unloading case. The results also indicate that the resistance decreases over cyclic loading. This is the case for both the resistance at full loading to 100% strain as well as in the unloaded configuration.

### B. Proximity Sensor

The straightforward use of the phototransistors to detect local occlusions lets a robot evaluate a low-resolution visual image of its local environment (Figure 5A).

In a context with many such robots entangling [5], [7], it would be desirable for these sensors to provide a measure of the degree of entanglement or the sensor’s position (surface vs. interior) in the entangled “blob”, based on occlusion by other robots in the blob. We test this use case with eight non-sensorized robots entangling around a single sensorized one (Figure 5B–D).

The masked area of the sensorized robot is divided into five equal segments to track the locally visible surface in each segment during entanglement. We define a measure of visibility as

$$v_i(t) = \frac{A_i(t)}{\max(A_i(t))} \quad (3)$$

with  $A_i(t)$  being the visible surface of segment  $i$  at time  $t$ . Thus  $v_i = 0$  would indicate that the segment of the robot is completely visible (unentangled) while  $v_i = 1$  would indicate the segment is completely obscured (as when buried in the interior of the entangled blob). We actuate the non-sensorized robots cyclically to entangle the sensorized robot 36 times while tracking the sensorized robot with the camera.

Figure 5D shows that the signal from the phototransistor and the visibility of the corresponding segment only correlate slightly, with  $\rho = 0.12$ . That is, with the setup tested here (in particular, the number and placement of phototransistors and the number of other robots), the exteroceptive sensing provides little information about the entanglement state.

### C. Sensor Compliance

A critical aspect of embedded sensing for soft robotics is the compliance of sensors. The integrated wires for the exteroceptive sensing are flexible, but introduce an inelastic element and therefore can be expected to affect the robot’s compliance. To quantify this effect, we compared non-sensorized robots, robots with only interoceptive carbon microparticle sensors, and fully sensorized robots, regarding their deformation at different operating pressures. Figure 6 indicates that even the interoceptive sensors increase the required operating pressure to achieve a given deformation. More prominent is the reinforcement effect for fully sensorized robots due to the limited elasticity of the wires. This significantly increases the required operating pressure for deformations larger than  $70^\circ$ . In the case of a deformation of  $120^\circ$ , the operating pressure for proprioceptive robots is 13% higher, and for fully sensorized robots 38% higher, than for a robot without sensors.

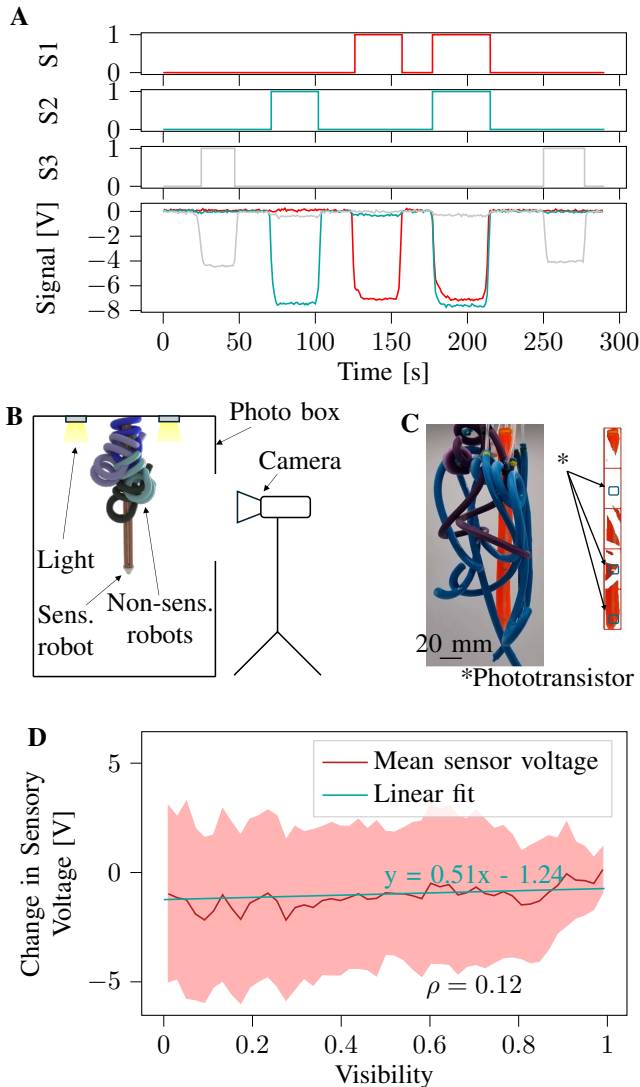


Fig. 5: Experimental tests of exteroceptive sensing. (A) Component test of sensing with phototransistors. The binary traces (S1–S3) indicate during which period a phototransistor has been covered by manually placing another robot at this location. (B–D) Entanglement sensing using exteroceptive sensors. (B) One sensorized and eight non-sensorized robots are placed in a photo box, with one set of phototransistors of the sensorized robot facing toward a camera. The non-sensorized robots entangle the sensorized one, occluding some phototransistors. (C) Raw image and processed visible area of the sensorized robot, separated into five segments for local resolution of entanglement at the locations of phototransistors. (D) Sensor and tracking measurements of entanglement show only a weak correlation between the visibility of the segment around a phototransistor and its voltage signal. The filled area shows the change in sensory voltage within one standard deviation.

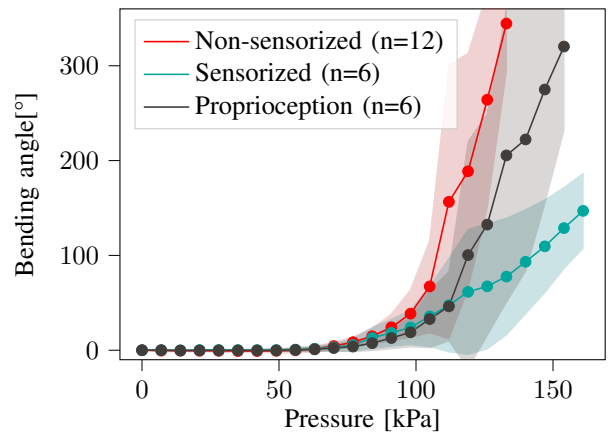


Fig. 6: Mechanical stiffening effect from sensorizing high-aspect-ratio soft pneumatic actuators. The plot shows the tested samples’ mean deformation and area within one standard deviation.

TABLE I: Comparison of sensor mechanisms considered in this work. Reduction in compliance: ○ = little or no effect, ◐ = moderate effect, ● = major effect.

	Signal-to-Noise Ratio	Reduction in Compliance
<b>Interoceptive Sensing</b>		
Optical Proprioception Sensor	0.0370	●
1-Thread (Self-Capacitive) Proprioception Sensor	5.330	○
2-Thread (Mutual Capacitive) Proprioception Sensor	488.3	●
Carbon Microparticle Strain Sensor	34.16	○
<b>Exteroceptive Sensing</b>		
Self-Capacitive Sensing	1.076	●
Phototransistor Imaging	19.22	◐

#### D. Alternate Sensing Mechanisms

Before settling on the design described above, we explored two other potential approaches to proprioceptive and external sensing. One was based on an interoceptive optical sensor, intended to give information about pose (degree of curling). The other was based on capacitive sensing, potentially of use for both purposes. Here, we outline those approaches and the reasons we did not use them in the final version of the design.

The interoceptive optical sensor consisted of an internal LED at one end of the robot’s body and a phototransistor at the other end, with the body acting as an optical waveguide in between [17]. The macrobending effect of the waveguide reduces light intensity according to the degree of bending of the body.

We tested capacitive proprioception sensors in two forms. The first consisted of a single integrated conductive thread running the length of the body. Such a thread could potentially be used as a proximity sensor, based on capacitive changes resulting from nearby conductive objects or other robots, or as a proprioception sensor based on forming an

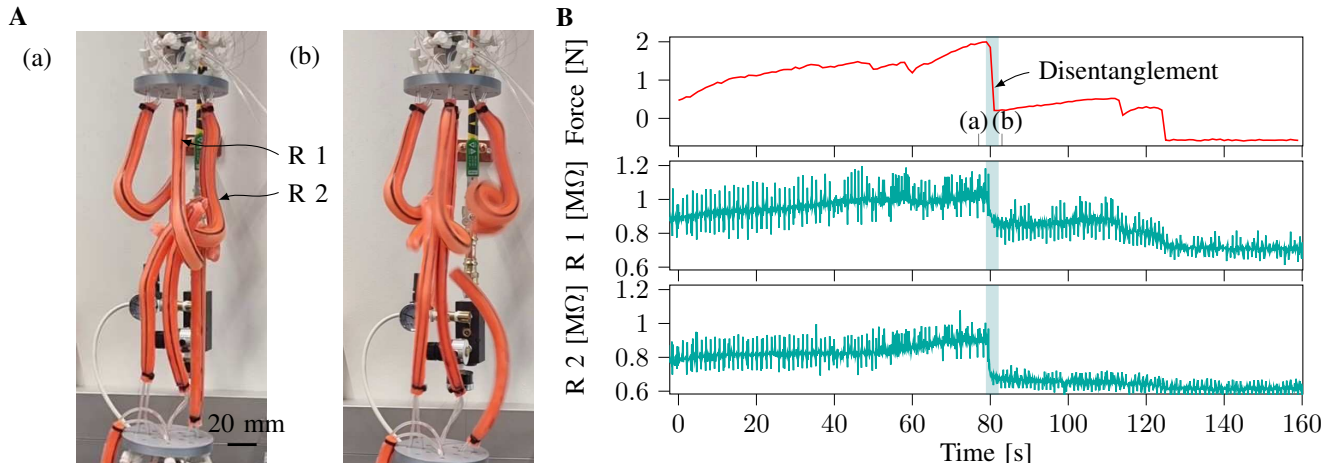


Fig. 7: Grip failure test, in which two sets of entangled robots are pulled apart using a tensile test machine (Instron 68TM-10). (A) Snapshots of a trial with eight entangled robots separating under load. Robots R1 and R2 provide the proprioceptive sensor signals shown in panel B. The points in time (a) and (b) in the upper plot of panel B indicate the times of the snapshots. (B) Time course of applied force and proprioceptive sensor measurements for two of the upper four robots during the test. As the machine separates the entangled robots, they are gradually pulled into a straighter configuration, and the proprioceptive resistance measurement slowly increases. When pulled free from the entanglement, the robots return quickly to a curled position, showing sudden changes in proprioceptive resistance measurements, while the entanglement force recorded by the tensile test machine simultaneously drops.

inductive coil under actuation. The second form consisted of two conductive threads wrapped helically around the actuator, which separate under body deformation, resulting in a decreasing capacitance [21].

We tested these sensors, as well as the others described in previous sections, by measuring their Signal-to-Noise ratio (SNR) for actuation up to a complete  $360^\circ$  loop as a quantitative metric of sensor performance. We also qualitatively evaluated each sensor according to its effect on the robot’s compliance. The results are reported in Table I. The combination of both considerations led to the choice of sensors in the final version of the robot, as described earlier.

We found that interoceptive optical sensors suffered from the translucency of the silicone rubber, even when coloring was added to darken it as much as possible and isolate internal from external light. Mutual capacitive sensors showed the highest SNR by an order of magnitude, but capacitive sensors are highly affected by external EMF signals. Furthermore, the inelastic electrodes reinforce the actuator and reduce the deformation range significantly (see supplementary video). Self-capacitive sensors had low SNR, as well as difficulty distinguishing signals resulting from proximity to an external object from those resulting from curling.

## V. TOWARDS APPLICATIONS

High-aspect-ratio soft robots have potential applications in areas including grasping, locomotion, manipulation, and artificial muscles. In this section, we outline potential uses of robots with integrated sensing in the first two of those areas.

### A. Failure Detection in Stochastic Entanglement Grasping

To explore how proprioception could aid grasping, we performed experiments in which sets of robots were attached to the plates of a tensile test machine, pressurized to entangle, and slowly pulled apart (Figure 7). As individual robots lose contact and are pulled free of the entanglement (thereby weakening the grip), the resulting sudden configuration change is apparent in their proprioceptive measurements. In this way, integrated proprioception sensors could provide information about impending grasp failures for soft grippers, such as entanglement grippers with high-aspect-ratio tendrils [5].

### B. Autonomous Role Differentiation for Collective Locomotion of Worm-Inspired Soft Robots

California blackworms can entangle into “blobs” that exhibit collective locomotion, where worms adopt different roles (“pullers”, “wigglers”, etc.) based on their location within the blob [13]. A system of robots inspired by the worms has similarly demonstrated collective locomotion [7]. In that latter work, robots are manually assigned roles based on their location. Sensors like those presented here could provide information to each robot to help it determine its location within the blob, and choose a role and gait accordingly. For instance, a robot that changes its actuation state without registering a corresponding change in proprioceptive signal is likely to be immobilized by being entangled by other robots; a robot sensing a bright external light is likely to be on the leading face of a blob performing phototaxis. We will investigate such strategies in future work.

## VI. CONCLUSION

In this work, we developed a design and manufacturing process for interoceptive and exteroceptive sensors in high-aspect-ratio soft robots. Carbon microparticle proprioceptive sensors detect the robot's deformation even for high bending angles. Exteroceptive sensing with distributed phototransistors allows the detection of external obstacles based on occlusion.

In our tests, the exteroceptive sensor was insufficient to provide reliable information about a robot's entanglement state. It is possible that the phototransistor array would be more effective as an entanglement sensor if there were a larger number of robots, so that interior locations were more fully occluded from ambient light. A larger number of phototransistors could also be useful in providing a higher-resolution evaluation of the local environment. More work is needed to explore these possibilities and increase the exteroceptive sensing's utility as an entanglement sensor.

Future work will also more thoroughly explore the uses outlined in Section V, testing grasp failure detection with a range of different objects and different numbers of robots, and advancing fully autonomous collective locomotion of worm-inspired robot swarms.

## ACKNOWLEDGEMENT

We thank Michelle C. Yuen for advising on interoceptive sensing, Carina Käser and Greg Freeburn for assisting with the experimental setups, and Rachel Zoll for helping with the laser cutting operations. Mirco Theile was supported by the Chair for Cyber-Physical Systems in Production Engineering at TUM and the Alexander von Humboldt Foundation.

## REFERENCES

- [1] R. F. Shepherd, F. Ilievski, W. Choi, S. A. Morin, A. A. Stokes, A. D. Mazzeo, X. Chen, M. Wang, and G. M. Whitesides, "Multigaît soft robot," *Proceedings of the National Academy of Sciences*, vol. 108, no. 51, p. 20400–20403, Nov. 2011.
- [2] S. Li, D. M. Vogt, D. Rus, and R. J. Wood, "Fluid-driven origami-inspired artificial muscles," *Proceedings of the National Academy of Sciences*, vol. 114, no. 50, p. 13132–13137, Nov. 2017.
- [3] A. Rafsanjani, Y. Zhang, B. Liu, S. M. Rubinstein, and K. Bertoldi, "Kirigami skins make a simple soft actuator crawl," *Science Robotics*, vol. 3, no. 15, p. eaar7555, Feb. 2018.
- [4] D. Rus and M. T. Tolley, "Design, fabrication and control of soft robots," *Nature*, vol. 521, no. 7553, pp. 467–475, May 2015.
- [5] K. Becker, C. Teeple, N. Charles, Y. Jung, D. Baum, J. C. Weaver, L. Mahadevan, and R. Wood, "Active entanglement enables stochastic, topological grasping," *Proceedings of the National Academy of Sciences*, vol. 119, no. 42, p. e2209819119.
- [6] J. Paek, I. Cho, and J. Kim, "Microrobotic tentacles with spiral bending capability based on shape-engineered elastomeric microtubes," *Scientific Reports*, vol. 5, no. 1, Jun. 2015.
- [7] C. Kaeser, J. Kwon, E. Challita, H. Tuazon, R. J. Wood, S. Bhamla, and J. Werfel, "Individual and collective behaviors in soft robot worms inspired by living worm blobs," *2025 IEEE International Conference on Robotics Automation (ICRA)*, May 2025.
- [8] T. J. Jones, E. Jambon-Puillet, J. Marthelot, and P.-T. Brun, "Bubble casting soft robotics," *Nature*, vol. 599, no. 7884, p. 229–233, Nov. 2021.
- [9] R. V. Martinez, J. L. Branch, C. R. Fish, L. Jin, R. F. Shepherd, R. M. D. Nunes, Z. Suo, and G. M. Whitesides, "Robotic tentacles with three-dimensional mobility based on flexible elastomers," *Advanced Materials*, vol. 25, no. 2, p. 205–212, Sep. 2012.
- [10] F. Meder, S. P. Murali Babu, and B. Mazzolai, "A plant tendril-like soft robot that grasps and anchors by exploiting its material arrangement," *IEEE Robotics and Automation Letters*, vol. 7, no. 2, p. 5191–5197, Apr. 2022.
- [11] X. Guo, W. Tang, K. Qin, Y. Zhong, H. Xu, Y. Qu, Z. Li, Q. Sheng, Y. Gao, H. Yang, and J. Zou, "Powerful uav manipulation via bio-inspired self-adaptive soft self-contained gripper," *Science Advances*, vol. 10, no. 19, May 2024.
- [12] J. Frás, M. Macias, Y. Noh, and K. Althoefer, "Fluidical bending actuator designed for soft octopus robot tentacle," *2018 IEEE International Conference on Soft Robotics (RoboSoft)*, vol. 73, p. 253–257, Apr. 2018.
- [13] Y. Ozkan-Aydn, D. I. Goldman, and M. S. Bhamla, "Collective dynamics in entangled worm and robot blobs," *Proceedings of the National Academy of Sciences*, vol. 118, no. 6, p. e2010542118, Feb. 2021.
- [14] K. P. Becker, Y. Chen, and R. J. Wood, "Mechanically programmable dip molding of high aspect ratio soft actuator arrays," *Advanced Functional Materials*, vol. 30, no. 12, p. 1908919, Mar. 2020.
- [15] T. G. Thuruthel, B. Shih, C. Laschi, and M. T. Tolley, "Soft robot perception using embedded soft sensors and recurrent neural networks," *Science Robotics*, vol. 4, no. 26, Jan. 2019.
- [16] S. Wang, Z. Sun, Y. Zhao, and L. Zuo, "A highly stretchable hydrogel sensor for soft robot multi-modal perception," *Sensors and Actuators A: Physical*, vol. 331, p. 113006, Nov. 2021.
- [17] H. Bai, S. Li, J. Barreiros, Y. Tu, C. R. Pollock, and R. F. Shepherd, "Stretchable distributed fiber-optic sensors," *Science*, vol. 370, no. 6518, p. 848–852, Nov. 2020.
- [18] M. C. Yuen, R. Kramer-Bottiglio, and J. Paik, "Strain sensor-embedded soft pneumatic actuators for extension and bending feedback," *2018 IEEE International Conference on Soft Robotics (RoboSoft)*, vol. 24, p. 202–207, Apr. 2018.
- [19] H. A. Sonar, M. C. Yuen, R. Kramer-Bottiglio, and J. Paik, "An any-resolution pressure localization scheme using a soft capacitive sensor skin," *2018 IEEE International Conference on Soft Robotics (RoboSoft)*, vol. 110, p. 170–175, Apr. 2018.
- [20] C. Ge, B. Yang, L. Wu, Z. Duan, Y. Li, X. Ren, L. Jiang, and J. Zhang, "Capacitive sensor combining proximity and pressure sensing for accurate grasping of a prosthetic hand," *ACS Applied Electronic Materials*, vol. 4, no. 2, p. 869–877, Jan. 2022.
- [21] H. Kim, H. Na, S. Noh, S. Chang, J. Kim, T. Kong, G. Shin, C. Lee, S. Lee, Y.-L. Park, S. Oh, and J. Lee, "Inherently integrated microfiber-based flexible proprioceptive sensor for feedback-controlled soft actuators," *npj Flexible Electronics*, vol. 8, no. 1, Mar. 2024.
- [22] T. Lee, R. Kashyap, and C. Chu, "Building skeleton models via 3-d medial surface axis thinning algorithms," *CVGIP: Graphical Models and Image Processing*, vol. 56, no. 6, p. 462–478, Nov. 1994.